

# Assessment of a Novel Flow Visualization Technique Using Photodissociation Spectroscopy

YAN ZHAO, CHENNING TONG, and LIN MA\*

*Department of Mechanical Engineering, Clemson University, Clemson, South Carolina 29634-0921*

The study of complicated flows continuously calls for new nonintrusive flow diagnostics. A novel flow visualization technique based on photodissociation spectroscopy (PDS) is described, demonstrated, and assessed in this paper. This technique is centered around the creative use of photodissociation (PD). A PD precursor is seeded in the flow of interest, either passive or reactive. A laser pulse is then generated to completely and rapidly photodissociate both the precursor and the products formed from the precursor (if it reacts) into photofragments. A target photofragment is then imaged to obtain multidimensional information about the flow. An analytical methodology was developed to assess the feasibility of the PDS-based technique. This analytical method was applied to the case where molecular iodine was used as an example PD precursor, and the results were validated by experimental data. Both the analytical and experimental findings provided a promising outlook for this new technique as a practical flow visualization technique. With a properly chosen PD precursor, the PDS-based technique provides an attractive alternative for imaging several critical flow properties, including the mixture fraction and temperature field. This technique shares some key advantages with established techniques, e.g., a high spatial and temporal resolution comparable to the planar laser-induced fluorescence (PLIF) technique. Meanwhile, this technique offers several unique advantages to overcome the limitations of existing techniques, including enhancing the signal level and simplifying the interpretation of the signal.

Index Headings: **Optical sensing; Flow imaging; Photodissociation spectroscopy.**

## INTRODUCTION

In the study of a wide spectrum of flows, there is a critical need for a nonintrusive technique capable of quantitatively visualizing the concentration and distribution of chemical species. An important example involves the ongoing study of the complicated interaction between turbulence and chemical reactions, which governs the operation, stability, and pollutant formation of most practical combustion devices.<sup>1,2</sup> In this example, it is highly desirable to “track” the turbulent mixing process and chemical reactions by imaging the concentration of one or more chemical species.

Such imaging needs pose significant challenges for well-established laser visualization techniques, such as Rayleigh scattering, Raman scattering, planar laser-induced fluorescence (PLIF), and absorption tomography techniques. The application of Rayleigh scattering is usually limited to passive flows because it is not species specific. In reactive flows, many intermediate and new species are present and can obscure, or even prevent, a meaningful interpretation of the Rayleigh signal.<sup>3</sup> The application of Raman scattering is mainly limited by its relatively low signal level, which is lower than Rayleigh scattering by a factor of about  $10^3$ . Consequently, obtaining two-dimensional (2D) Raman images is impractical for most

applications.<sup>3</sup> Furthermore, due to their nonresonant nature or the weak signal, both Rayleigh and Raman scattering are susceptible to interferences such as Mie scattering. Being a resonant technique, PLIF offers higher signal level and is perhaps the most extensively applied visualization technique in reactive flows.<sup>3–5</sup> However, PLIF is not well suited for tracking the mixing and reaction processes. The best established species for PLIF application include OH, NO, and acetone. However, OH and NO only exist in limited regions of certain reactive flows, and they undergo chemical reactions themselves in most combustion flows, and acetone does not naturally exist in most flows and its application in combustion flows is plagued by pyrolysis. In absorption tomography, many line-of-sight-averaged absorption measurements are performed at multiple locations across the flow of interest. A mathematical inversion is then performed to reconstruct the flow structure, e.g., the temperature and species distribution,<sup>6,7</sup> based on these measurements. Being species specific and offering stronger signal, absorption tomography overcomes some of the aforementioned limitations; but it cannot provide the required spatial resolution to resolve the flow structure in most cases.

This current work assesses the feasibility of a new flow visualization technique based on photodissociation (PD). This technique involves seeding a PD precursor into the flow of interest, which is rapidly and completely photodissociated into photofragments using a laser pulse. The concentration of an easily detectable photofragment is then imaged (typically via PLIF) to visualize the flow. This technique based on photodissociation spectroscopy (PDS) overcomes the limitations of existing techniques discussed above. Firstly, this technique shares the key virtues of PLIF (e.g., high signal level, high spatial resolution, and species specificity) and offers several new ones. By selecting a PD precursor that produces a photofragment (e.g., an atomic species) with a strong LIF transition, this technique can provide even higher signal level than the existing PLIF technique and can potentially simplify the interpretation of the signal. Furthermore, if the target photofragment does not naturally exist in the flow of interest, its concentration represents a conserved scalar, which can be used to track the mixing and reaction processes. These new advantages show great promise to extend the applicable range of traditional PLIF techniques.

In this paper, the feasibility and applicable range of the PDS technique is analyzed both analytically and experimentally using molecular iodine ( $I_2$ ) as an example PD precursor. The measurement concept and theoretical background relevant to the PDS of  $I_2$  are first introduced. Key aspects of the new technique, in terms of its detectivity, spatial resolution, and signal strength, are assessed both analytically and experimentally. Finally, the paper is closed with conclusions and an outlook.

Received 19 September 2008; accepted 3 December 2008.

\* Author to whom correspondence should be sent. E-mail: LinMa@clemson.edu.

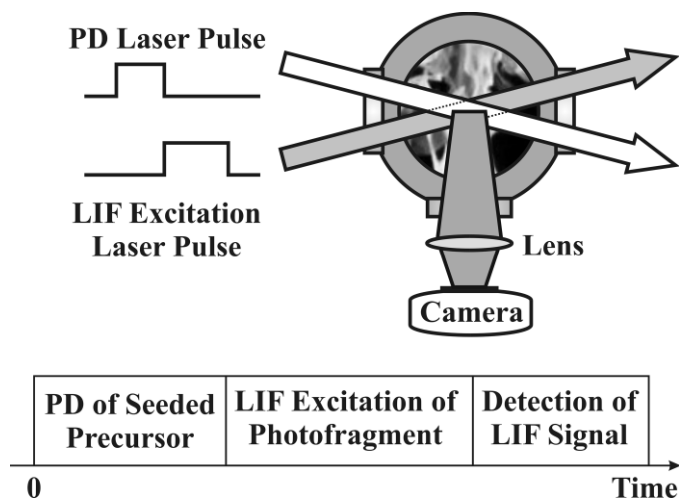


FIG. 1. The concept of flow imaging using PDS.

## DESCRIPTION OF THE NEW IMAGING CONCEPT

Molecules can be dissociated into fragments by absorbing photons, a process named photodissociation (PD). Such photofragments, when in atomic form, are especially attractive for PLIF imaging because of their strong LIF transition strength and structural simplicity. A possible approach to utilize the PDS for flow imaging is conceptually depicted in Fig. 1. The imaging technique utilizes the PD of a precursor seeded into the flow of interest. A laser pulse, labeled as the “PD Laser Pulse” in Fig. 1, rapidly and completely photodissociates the precursor (and the products formed from the precursor if it reacts) into photofragments (atoms) within the pulse duration. The concentration of a photofragment represents a conserved scalar, which can be used to track the mixing and reaction processes if (1) one of the resulting atoms does not naturally exist in the flow, and (2) it is imaged before its distribution is changed by the flow or by chemical reactions. The first condition can be satisfied by carefully selecting a PD precursor, as discussed later, and the second condition can usually be satisfied by imaging the target photofragment using the PLIF technique as shown. A second laser pulse, labeled as the “LIF Excitation Laser Pulse”, is generated after the PD laser pulse to excite the target photofragment produced in the PD process, and PLIF images of the target atoms are subsequently obtained. The timing scheme at the lower part of Fig. 1 summarizes the measurement sequence and the imaging concept. With a well-selected precursor, our calculations have shown that complete PD can be achieved within a few nanoseconds using readily available laser equipment. The timescale for LIF excitation and detection is typically less than tens of nanoseconds,<sup>3</sup> during which the concentration of the target photofragment essentially remains frozen. The total measurement time of the technique is, therefore, on the order of tens of nanoseconds, short enough to resolve the smallest time scale encountered in almost all current research.<sup>2,8</sup>

The imaging concept is better explained by using an example in which molecular iodine,  $I_2$ , is seeded as the precursor in the fuel stream of a hydrocarbon/air flame. Extensive calculations using the GRI-Mechanism 3.0,<sup>9</sup> and the reaction mechanism of  $I_2$ ,<sup>10,11</sup> showed that, when seeded in hydrocarbon/air flames,  $I_2$  reacts to form HI, and atomic I.

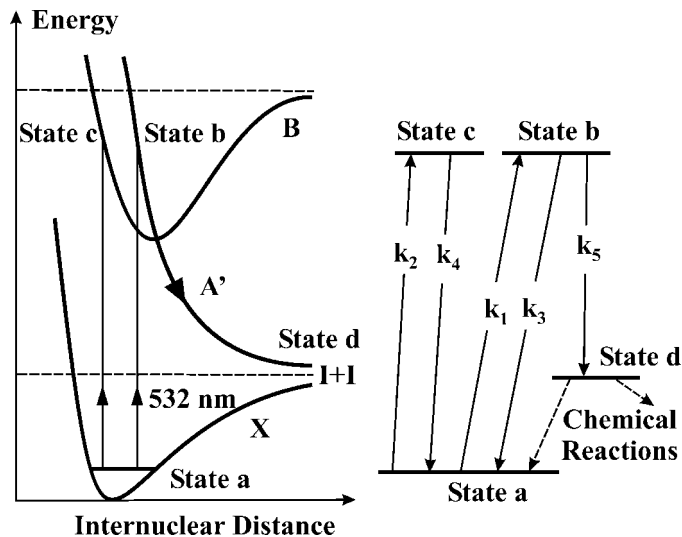


FIG. 2. (Left) Potential curves of  $I_2$  (not to scale) relevant to the PD at 532 nm. (Right) A four-state kinetic model describing the PD dynamics.

Therefore, if both  $I_2$  and HI can be completely photodissociated, then the seeded  $I_2$  is completely converted into atomic I in the flow. Hence, imaging of atomic I will provide a conserved scalar (the mixture fraction<sup>1</sup>) in the flow to study turbulent mixing and reaction. The complete PD of  $I_2$  and HI, and the subsequent imaging of atomic I, are assessed in the next two sections, respectively.

## ASSESSMENT OF COMPLETE PHOTODISSOCIATION

As described above, the PDS technique depends on the ability to completely photodissociate the seeded precursor and its possible products. The complete PD of  $I_2$  and HI can be accomplished with commonly used lasers. Both  $I_2$  and HI exhibit significant PD cross-sections in a wide spectral range.<sup>12,13</sup> In the visible, significant PD of  $I_2$  starts around 700 nm, peaks at 533 nm, and extends to approximately 422 nm.<sup>14</sup> In the ultraviolet (UV), PD of  $I_2$  has been demonstrated at 193<sup>15</sup> and 266 nm.<sup>16</sup> For HI, significant PD starts near 300 nm, reaches a maximum at approximately 222 nm, and extends to the vacuum ultraviolet (UV).<sup>17</sup> Here we examined the PD of  $I_2$  and HI at three wavelengths where both of them have relatively large PD cross-sections: 532, 266, and 248 nm, corresponding to the second and fourth harmonics of the Nd:YAG lasers, and the output of the KrF excimer lasers, respectively.

We first describe the models to analyze the completeness of PD, using the PD of  $I_2$  at 532 nm as an example. The left part of Fig. 2 shows three potential curves of  $I_2$  relevant to its PD at 532 nm. Through stimulated absorption, photons at 532 nm excite  $I_2$  from its  $X(^1\Sigma_g^+)$  ground state (State a) to the excited state  $A'(^1\Pi_{1u})$  (State b) and  $C(^3\Pi_{0u}^+)$  (State c). State b is repulsive and dissociates spontaneously into two I atoms (state d) very rapidly, on the order of 100 femtoseconds.<sup>18,19</sup> State c is not repulsive and can only predissociate, but the predissociation rate is too slow to be considered here.<sup>20</sup> Meanwhile, both State b and State c will be deactivated to State a by stimulated emission. Moreover, these four states are also coupled by spontaneous emission, collisional quenching, and chemical reactions. However, at the laser intensity and time

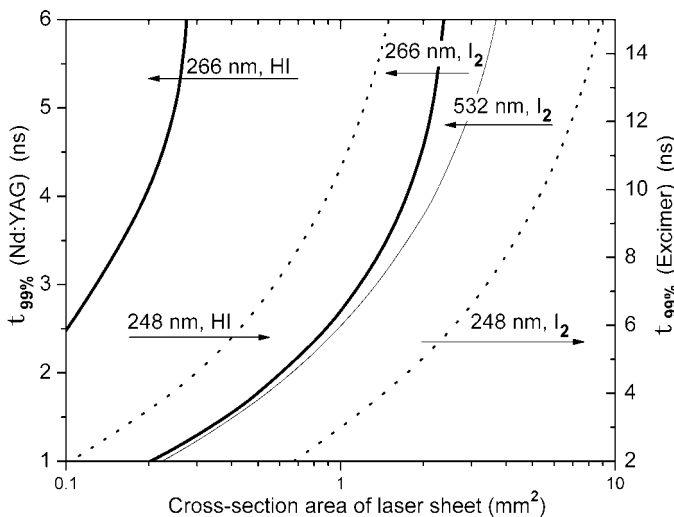


FIG. 3. Time to reach 99% PD of I<sub>2</sub> and HI at different wavelengths. The temporal profile of laser pulses is assumed to be Gaussian, with parameters provided by laser manufacturers.

scale considered here, these effects are negligible compared to those laser-induced effects and the spontaneous dissociation.

With the above understanding, a four-level kinetic model is developed to analyze the PD of I<sub>2</sub> at 532 nm, depicted in the right part of Fig. 2 and described by the following mechanism:

Stimulated absorption from State a to b:



Stimulated absorption from State a to c:



Stimulated emission from State b to a:



Stimulated emission from State c to a:



Spontaneous dissociation of State b to d:



$$k_1 = \frac{i\sigma_{ab}\lambda}{hc}; \quad k_2 = \frac{i\sigma_{ac}\lambda}{hc}; \quad k_3 = \frac{g_a}{g_b}k_1; \quad (6)$$

$$k_4 = \frac{g_a}{g_c}k_2; \quad k_5 \cong 10^{13} \text{ s}^{-1}$$

Here,  $I_2^*(b)$  and  $I_2^*(c)$  denote excited I<sub>2</sub> molecules in State b and c, respectively;  $k_1$  to  $k_5$  are the rate coefficients ( $\text{s}^{-1}$ ) for transition (1) to (5) (value of  $k_5$  taken from Refs. 18 and 19);  $\sigma_{ab}$  and  $\sigma_{ac}$  are the absorption cross-sections ( $\text{cm}^2$ ) for the transition from State a to b and State a to c, respectively;  $i$  is the laser radiance ( $\text{W}/\text{cm}^2$ );  $\lambda$  is the wavelength (nm);  $g_a$ ,  $g_b$ , and  $g_c$  are the degeneracy of State a, b, and c, respectively; and  $h$  and  $c$  are Planck's constant and the speed of light in appropriate units. This mechanism captures the major physics

of the PD dynamics of I<sub>2</sub> at 532 nm.<sup>21</sup> For the photodissociation of I<sub>2</sub> at a wavelength of 532 nm, the following parameters were used:  $\sigma_{ab} = 1.12 \times 10^{-19} \text{ cm}^2$  and  $\sigma_{ac} = 7.5 \times 10^{-19} \text{ cm}^2$ , respectively;<sup>14,22</sup>  $g_a/g_b = 1$  and  $g_a/g_c = 1$ .<sup>23</sup>

This mechanism leads to a set of rate equations, coupling the populations at States a to d:

$$\frac{dN_a}{dt} = -k_1N_a - k_2N_a + k_3N_b + k_4N_c \quad (7a)$$

$$\frac{dN_b}{dt} = k_1N_a - k_3N_b - k_5N_b \quad (7b)$$

$$\frac{dN_c}{dt} = k_2N_a - k_4N_c \quad (7c)$$

$$\frac{dN_d}{dt} = k_5N_b \quad (7d)$$

where  $N_a$ ,  $N_b$ ,  $N_c$ , and  $N_d$  stand for the fraction of the I atoms in States a, b, c, and d, respectively. Note that in the calculation of fraction, two I atoms were counted as one I<sub>2</sub> molecule. The initial conditions for these rates equations are

$$N_a|_{t=0} = 100\%, \quad N_b|_{t=0} = N_c|_{t=0} = N_d|_{t=0} = 0 \quad (8)$$

These equations are solved numerically to obtain the temporal evolution of the population in each state. A characteristic time,  $t_{99\%}$  (ns), is then defined as the time when the number of I atoms in State d reaches 99% of the total number of I atoms in the system; or equivalently, the time when 99% of the I<sub>2</sub> molecules in the system have been photodissociated into I atoms. Obviously,  $t_{99\%}$  quantifies the rapidness to achieve "complete" PD: a small  $t_{99\%}$  indicates that the complete PD requires a short period of time, and vice versa. Our study shows that  $t_{99\%}$  depends strongly on the laser radiance and the absorption cross-sections and weakly on the temporal profile of the laser pulse, evidenced by the insensitivity of  $t_{99\%}$  with respect to the full width at half-maximum (FWHM) of the Gaussian profiles used.

An example calculation of  $t_{99\%}$  is shown in Fig. 3 for the PD of I<sub>2</sub> at 532 nm using a Nd:YAG laser, assuming the laser pulses are transformed into a laser sheet. Therefore, for a fixed pulse energy (500 mJ per pulse) and temporal profile of the pulse (assumed to be Gaussian with an 8 ns FWHM), the laser radiance depends only on the cross-section area of the laser sheet. Parameters for the photodissociation of I<sub>2</sub> at a wavelength of 532 nm are those mentioned earlier, and parameters for the photodissociation of HI at the UV wavelengths are taken from Refs. 23 and 24. The results obtained are shown by the thin solid line labeled "532 nm, I<sub>2</sub>". Clearly,  $t_{99\%}$  decreases with the cross-section area of the laser sheet, due to the enhanced transition rates brought about by the increased radiance. Figure 3 shows that a  $t_{99\%}$  of 6 ns corresponds to a cross-section area of about 3.7 mm<sup>2</sup> in this case. Therefore, at a typical laser sheet thickness of 0.2 mm, 99% PD of I<sub>2</sub> can be achieved within 6 ns across a height of approximately 18 mm using a laser with moderate power, which provides a quite large field of view for subsequent imaging.

Similar models were built to analyze the PD of I<sub>2</sub> at other wavelengths and the PD of HI. Figure 3 also shows the analysis for the PD of I<sub>2</sub> and HI at 266 and 248 nm. These

wavelengths effectively photodissociate both  $I_2$  and  $HI$ <sup>12,13</sup> and can be conveniently generated using Nd:YAG and KrF excimer lasers. Here, the pulse energy is set at 100 mJ at 266 nm and 300 mJ at 248 nm. These results provide the dimension of the field-of-view for imaging atomic I using different PD lasers. At the wavelengths used here, the PD of HI limits this dimension. With the 266 nm laser, a  $t_{99\%}$  of 6 ns corresponds to a cross-section area of 0.27 mm<sup>2</sup> for HI, corresponding to a height of approximately 1.4 mm at a thickness of 0.2 mm. Therefore, this PD strategy is most suitable for line imaging, although larger fields of view can be obtained for 2D imaging by reducing the laser sheet thickness and by using more powerful lasers. The 248 nm laser pulses substantially enlarge the field of view due to the enhanced PD cross-section of HI at 248 nm over that at 266 nm<sup>24</sup> and the increased pulse energy generated by excimer lasers over that generated by Nd:YAG lasers. With the 248 nm laser, a  $t_{99\%}$  of 15 ns corresponds to a cross-section area of 1.5 mm<sup>2</sup> for HI, corresponding to a height of 7.5 mm at a thickness of 0.2 mm, which provides a reasonably large field of view for flow visualization. When needed, the field of view can be further enlarged by reducing the laser sheet thickness, by using more powerful lasers, and also by using lasers at wavelengths where HI exhibits a larger PD cross-section (e.g., 222 nm generated by the KrCl excimer laser, where HI's maximum PD cross-section is located). With these techniques, a field of view of a few centimeters can be obtained for 2D imaging.

In summary, the seeding of  $I_2$  as a precursor in typical hydrocarbon flames results in simple products, with only three iodine-containing species to be considered,  $I_2$ , HI, and atomic I. Both  $I_2$  and HI can be completely and rapidly photodissociated with commonly used lasers across a large field of view.

## ASSESSMENT OF THE IMAGING OF THE TARGET PHOTOFRAGMENT

This section assesses the imaging of the target photofragment, atomic iodine, generated by the PD process, in terms of the signal-to-noise ratio, spatial resolution, signal strength, and the size of the field of view. Atomic I has been detected using resonance enhanced multi-photon ionization,<sup>25</sup> vacuum UV LIF,<sup>26</sup> and two-photon LIF (TPLIF).<sup>27</sup> A survey of these techniques concluded that TPLIF provides the optimal strategy to image atomic I in practice because TPLIF avoids the use of vacuum UV wavelengths and provides a wide spectral separation between the LIF and the excitation wavelength.<sup>3</sup>

A summary of the TPLIF theory is provided here to facilitate the assessment. The rate at which TPLIF photons are collected by an imaging system,  $R$  (photons/s), is expressed as:

$$R(T) = \eta \cdot \frac{\Omega}{4\pi} \cdot V \cdot N_I \cdot W_{2\nu}(T) \cdot \frac{A}{A + Q + W_i(T)} \quad (9)$$

where  $T$  represents time,  $\eta$  is the quantum efficiency of the imaging system,  $\Omega$  is the collection solid angle;  $V$  is the collection volume (cm<sup>3</sup>);  $N_I$  is the number density of I atoms (cm<sup>-3</sup>);  $W_{2\nu}$  is the two-photon absorption rate coefficient (s<sup>-1</sup>);  $A$  is the Einstein coefficient for spontaneous emission from the fluorescing state to the final state under consideration (s<sup>-1</sup>);  $Q$  is the collisional quenching rate coefficient (s<sup>-1</sup>); and  $W_i$  is the photoinization rate coefficient (s<sup>-1</sup>). The imaging signal level is directly represented by  $R$ . Moreover,  $W_{2\nu}$  and  $W_i$  are

expressed as

$$W_{2\nu}(T) = \frac{i^2(T) \cdot \alpha_{2\nu} \cdot \lambda}{hc} \quad (10a)$$

$$W_i(T) = \frac{i(T) \cdot \sigma_i \cdot \lambda}{hc} \quad (10b)$$

where  $i(T)$  is the radiance of the excitation laser pulse (W/cm<sup>2</sup>),  $W_{2\nu}$  is the two-photon absorption cross-section (cm<sup>4</sup>/W),  $\lambda$  is the excitation wavelength length (nm), and  $\sigma_i$  is the photoionization cross-section (cm<sup>2</sup>). When the laser pulse exhibits a top-hat temporal profile, the radiance,  $i$ , remains constant during the pulse duration and is simply given by  $i = E / (H \cdot t \cdot \Delta T)$ , where  $E$  is the pulse energy (J);  $\Delta T$  is the duration of the laser pulse (ns); and  $H$  is the height of the laser sheet (mm). The product,  $H \cdot t$ , represents the cross-section area of the laser sheet (mm<sup>2</sup>).

From geometrical optics, the following two relations can be derived for the collection angle ( $\Omega$ ) and the collection volume per pixel ( $V$ , cm<sup>3</sup>):

$$\frac{\Omega}{4\pi} = \frac{1}{16f_{\#}^2} \cdot \frac{M^2}{(M+1)^2}; \quad V = \frac{s^2}{M^2} t \quad (11)$$

where  $f_{\#}$  is the  $f$ -number of the imaging system,  $M$  is the magnification factor,  $s$  is the pixel size of the imaging camera ( $\mu$ m), and  $t$  is the thickness of the excitation laser sheet (mm).

The number of TPLIF photons collected per pixel is then obtained by integrating  $R(T)$  over the collection time as shown below:

$$N_P = \int_{T=0}^{\Delta T} R(T) dT \quad (12)$$

In practice, the collection time is usually gated to be on the same length as the pulse width ( $\Delta T$ ) of the excitation pulse to minimize interference emission.

Finally, under shot-noise-limited detection, the signal-to-noise ratio ( $SNR$ ) of the imaging is determined by

$$SNR = \sqrt{\eta N_P} \quad (13)$$

According to Eqs. 9 through 13, the assessment of the TPLIF imaging technique involves a series of convoluted tradeoffs. This assessment focuses on the detection limit ( $SNR$ ), signal strength ( $N_P$ ), spatial resolution ( $t$ ), and size of the field of view ( $H$ ) under a given laser and imaging configuration (i.e., fixed  $i(T)$ ,  $\Delta T$ ,  $\eta$ ,  $f_{\#}$ ,  $M$ , and  $s$ ), with a certain TPLIF transition (i.e., fixed  $A$ ,  $\alpha_{2\nu}$ ,  $\sigma_i$ , and  $\lambda$ ) and seeding density (i.e., fixed  $N_I$ ). The complication in designing an optimal TPLIF configuration can be illustrated by examining the dependence of  $N_P$  on the thickness ( $t$ ) and height ( $H$ ) of the laser sheet. A small  $t$  and large  $H$  are desirable to enhance the spatial resolution and field of view, respectively. However, a small  $t$  diminishes the collection volume and a large  $H$  reduces the radiance. Both effects reduce  $N_P$ , and consequently  $SNR$ . The assessment is further complicated by the relative magnitude of  $Q$  and  $W_i$ , as indicated by Eqs. 9 and 10, at different radiance levels.

We found a parameterized approach effective in mapping out such intertwined relationships. To illustrate the parameterized analysis, the performance of TPLIF imaging of atomic I was analyzed in the case of a top-hat excitation pulse profile. In

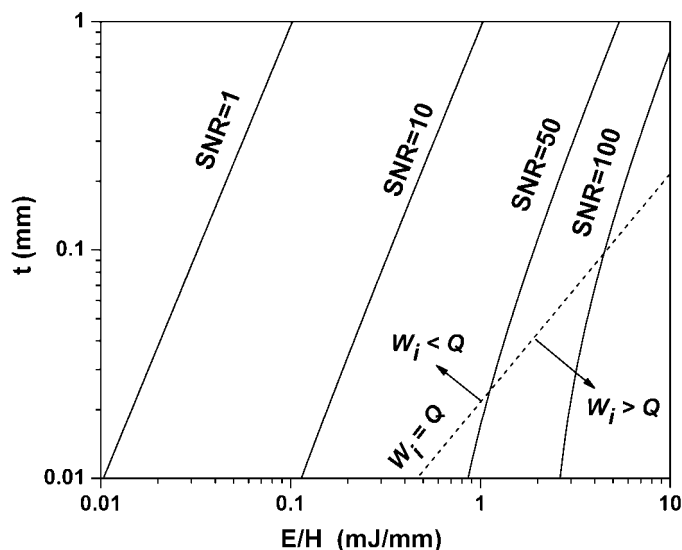


FIG. 4. Performance estimation of TPLIF imaging of atomic I. Parameters used:  $\eta = 80\%$ ,  $N_I = 3.7 \times 10^{15} \text{ cm}^{-3}$  (corresponding to a mole fraction of 0.1% at a temperature of 2000 K),  $A = 1 \times 10^7 \text{ s}^{-1}$ ,  $Q = 2 \times 10^9 \text{ s}^{-1}$  (hard-sphere calculation at a temperature of 2000 K),  $\alpha_{2v} = 1 \times 10^{-28} \text{ cm}^4/\text{W}$  (estimated from Ref. 25),  $\sigma_I = 2.3 \times 10^{-18} \text{ cm}^2$  (taken from Ref. 34),  $\lambda = 298 \text{ nm}$ ,  $f_{\#} = 1.4$ ,  $M = 1.6$ ,  $s = 26 \text{ } \mu\text{m}$ ,  $\Delta T = 8 \text{ ns}$ .

this case, the dependence of  $N_P$  on  $E$  and  $H$  can be grouped into the dependence on their ratio,  $E/H$ , as shown in Fig. 4. Figure 4 expounds the relationships between the spatial resolution ( $t$ ), the pulse energy, and the size of the field of view ( $E/H$ ), at different signal levels ( $SNR$ ). The two-photon transition from the  $5p^2P_{3/2}^0$  state to the  $6p^2P_{3/2}^0$  state at 298 nm (shown in the right panel of Fig. 5) was used in the calculation, and the TPLIF photons are emitted at 804.6 nm. The absorption of a third photon photoionizes I atoms at the  $6p^2P_{3/2}^0$  state. Other details of the calculation are shown in the caption of Fig. 4.

Figure 4 elucidates the interplay between these important factors at a temperature of 2000 K, simulating a combustion environment. First, at a fixed  $t$ , larger  $E/H$  is required to achieve higher  $SNR$ . In other words, more excitation energy is required at a certain field of view for higher detectivity. Second, at a fixed  $SNR$ ,  $E/H$  decreases with  $t$ . This suggests another advantage of small  $t$  besides improving spatial resolution, i.e., to reduce the  $E$  required to maintain a certain  $H$ . Third, a dotted line along which  $Q = W_i$  is also plotted to display their competition. In the region above this line,  $W_i$  is smaller than  $Q$ , a regime where collisional quenching dominates. In the region below this line,  $W_i$  becomes larger than  $Q$ , opening the possibility for quenching-independent measurement to remove the usual complexity in LIF of deciphering species- and temperature-dependent quenching rates.

Based on the above understanding, Fig. 4 can be employed to provide a concise and clear assessment of the TPLIF technique. For example, at a typical  $t$  of 0.2 mm, a TPLIF measurement with an  $SNR = 10$  requires an  $E/H \sim 0.5 \text{ mJ/mm}$ , i.e., an excitation pulse energy of 5 mJ across a field of view of 10 mm. Similarly, a measurement with an  $SNR = 50$  requires an  $E/H \sim 2.5 \text{ mJ/mm}$ , i.e., an excitation pulse energy of 25 mJ across a field of view of 10 mm. Both of these measurements will be dominated by collisional quenching.

Before leaving this section, note that (1) the assessment shown in Fig. 4 is conservative because the  $\alpha_{2v}$  used is a

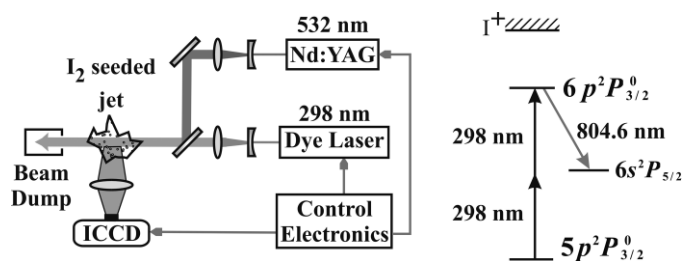


FIG. 5. Experimental setup to demonstrate the detection of atomic I using TPLIF.

conservative estimation from Ref. 27, and (2) the assessment is an “ideal” assessment because many practical factors have been neglected, such as the spectral overlap between the excitation pulse and the TPLIF transition, and the transmission efficiency of the lens. These practical factors will be considered in the experimental section.

## EXPERIMENTAL APPARATUS

To demonstrate the imaging concept and validate the analytical assessment provided above, the imaging concept introduced in Fig. 1 was experimentally implemented as shown in Fig. 5. In this implementation,  $I_2$  vapor was seeded as the PD precursor at 0.5% mole fraction to image the mixture fraction of a 4 mm air jet. The output at 532 nm from a Nd:YAG laser (Brilliant B), transformed into a laser sheet, acted as the “PD laser pulse” to completely photodissociate the seeded  $I_2$  into I atoms. The pulse energy of the 532 nm laser was approximately 400 mJ. A dye laser system (Sirah Cobra-Stretch pumped by a Quanta-ray Nd:YAG) was employed to generate the “LIF excitation laser pulse” at 298 nm, again transformed into a laser sheet spatially overlapping with the 532 nm laser sheet. The pulse energy of the 298 nm laser was about  $\sim 13 \text{ mJ}$ . Photons at 298 nm excite I atoms via a two-photon absorption process and TPLIF photons are emitted at 804 nm according to the energy diagram shown in the right panel,<sup>27</sup> which are imaged by an intensified charge-coupled device (ICCD) camera (Andor Technologies, DH734). The control electronics synchronize the operation of the lasers and the camera according to the timing scheme shown in Fig. 1. More specifically, the sequence of the imaging measurements is as follows: (1) a laser pulse at 532 nm, with a duration of approximately 8 ns, was generated to completely photodissociate the  $I_2$  molecules seeded in the flow; (2) another laser pulse at 298 nm, with a duration of approximately 8 ns, was subsequently generated to excite the I atoms produced in the first step; and finally, (3) the ICCD camera was triggered to collect the LIF photons with a gating time of 10 ns. Therefore, the total measurement time was on the order of tens of nanoseconds, sufficiently short to freeze most turbulent flows and chemical reactions. To confirm the completeness of the PD of the seeded  $I_2$ , the TPLIF signals at various PD laser energies were recorded and shown to be independent of the PD laser energies. A lens (Zeiss  $f/1.4$ , 85 mm) coupled with a set of close-up lenses (i.e.,  $f = 250 \text{ mm}$  and  $f = 500 \text{ mm}$ ) was applied to the camera to enhance the spatial resolution of the measurements.

To seed the  $I_2$  vapor in the flow, the air flow first passed through a vessel containing solid  $I_2$  beads before exiting to the jet. The vessel was maintained at a constant temperature to

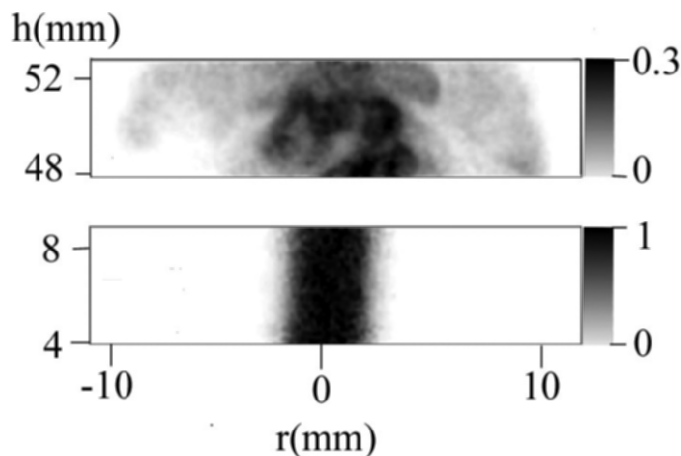


FIG. 6. Sample results for mixture fraction field near and far from the jet nozzle (image quality was degraded during file conversions).

control the vapor pressure of  $I_2$  vapor. By varying the vessel temperature and flow rate of the air, various concentrations of  $I_2$  vapor can be seeded into the jet. Drying agents were placed at the inlet of the vessel to ensure that the air was very dry to prevent forming iodic acid and coating the  $I_2$  beads, which inhibits the vaporization of the beads. A filter was placed at the outlet of the vessel to remove  $I_2$  dust to prevent interference Mie scattering in the measurements. Compared with other seeding techniques developed previously, e.g., the seeding of cesium<sup>28</sup> or xenon,<sup>29</sup> the seeding of  $I_2$  is considerably easier, safer, and less expensive.

## EXPERIMENTAL DEMONSTRATION AND ASSESSMENT

In these measurements, we demonstrated the use of the PDS-based technique for imaging the 2D mixture fraction. In a two-stream mixing process, the mixture fraction,  $\xi$ , is defined as

$$\xi = y/y_1 \quad (14)$$

where  $y$  represents a conserved quantity that is not changed by the flow or chemical reactions (e.g., the mass fraction of an element or an inert species—in our experiment, the concentration of atomic I); and  $y_1$  is the value of the conserved scalar in the first stream. Despite the simplicity of its definition, the mixture fraction plays a pivotal role in the study of many turbulent flows, and its measurements remain elusive despite the considerable research efforts invested.<sup>2</sup> The definition itself points to two possible measurement approaches, and both are challenging. The first approach measures the concentrations of all (at least the major) species present in the flow and then infers  $\xi$  using the mass fraction of an element.<sup>30</sup> The second approach measures the concentration of a seeded inert tracer (e.g., a fuel marker such as acetone<sup>4</sup> or  $NO^{31}$ ) and then infers  $\xi$  using the concentration of the tracer. However, these seeded inert tracers do not always remain “inert”. For example, both fuel markers and  $NO$  undergo chemical reactions (e.g., thermal dissociation caused by elevated temperatures in the flow).

The imaging technique based on PDS described here provides an alternative method of imaging  $\xi$ , which does not require the simultaneous 2D imaging of multiple species and is relatively more immune to chemical reactions. A set of sample results are shown in Fig. 6, at a Reynolds number of 2000.

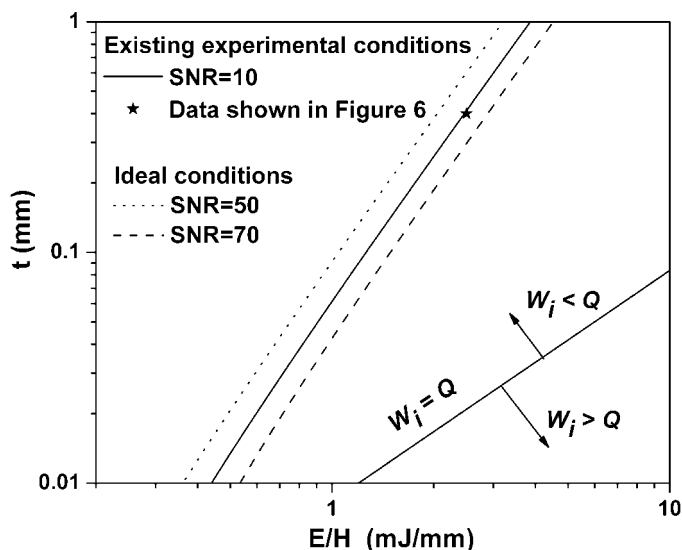


FIG. 7. Performance estimation of TPLIF imaging of atomic I. Parameters used:  $\eta_{\text{eff}} = 13\%$ ,  $\Phi = 0.2$ ,  $N_I = 2.5 \times 10^{16} \text{ cm}^{-3}$  (corresponding to a mole fraction of 0.1% at a temperature of 300 K), and  $Q = 5 \times 10^9 \text{ s}^{-1}$  (hard-sphere calculation at a temperature of 300 K).

Figure 6 displays the images of the mixture fraction of the jet at different jet heights, one near the jet exit and one far away from the jet exit where the turbulence was more developed.

Besides demonstrating the measurement concept, these measurements also provide an experimental validation of the analytical assessment described above. To apply the assessment method developed above, several practical factors need to be considered, with the most prominent two being the spectral overlap between the excitation pulse and the TPLIF transition, and the transmission efficiency of the lens. These two factors are incorporated as shown below:

$$R(T) = \eta_{\text{eff}} \cdot \frac{\Omega}{4\pi} \cdot V \cdot N_I \cdot W_{2\nu}(T) \cdot \frac{A}{A + Q + W_i(T)} \cdot \Phi \quad (15)$$

where  $\eta_{\text{eff}}$ , the effective quantum efficiency of the imaging system, combines the quantum efficiency of the ICCD and the transmission of the lens; and  $\Phi$  is the spectral overlap function.<sup>32</sup> With our existing experimental equipment,  $\eta_{\text{eff}}$  was estimated to be 0.13 (the ICCD was specified with a quantum efficiency of 0.17 at 804 nm, and the lens was estimated to have a transmission of 80% at 804 nm), and  $\Phi$  was estimated to be 0.2. The spectral overlap function,  $\Phi$ , was estimated using the method described in Ref. 32, with the linewidth of the laser taken to be  $0.05 \text{ cm}^{-1}$  and the linewidth of the TPLIF transition to be  $0.17 \text{ cm}^{-1}$ .<sup>33</sup>

The performance assessment of the measurements is shown in Fig. 7. Details of the parameters used are shown in the caption of Fig. 7. The parameters not shown are the same as those in the caption of Fig. 4. In the experiment, the thickness of the laser sheet was 0.4 mm and  $E/H$  was 2.6 mJ/mm (13 mJ of excitation energy over a 5 mm field-of-view). These conditions are indicated by the star symbol shown in Fig. 7. The  $SNR$  of the measurement was determined to be approximately 10. A calculation was conducted at an  $SNR = 10$  following the assessment method described in the section on the Assessment of the Imaging of the Target Photofragment, and the results are shown by the solid line. As can be seen, the

actual *SNR* of the experimental data was well estimated by the assessment method. The line along which  $W_i = Q$  is also shown here, indicating the domination of collisional quenching under the experimental conditions.

To explore potential improvement, an assessment under the “ideal” conditions (i.e., an  $\eta_{\text{eff}} = 0.8$  and a perfect overlap with  $\Phi = 1$ ) was also performed and plotted in Fig. 7. Practically, these ideal conditions can be realized by using a camera and lens with better quantum efficiency and transmission efficiency in the near infrared and by using a seeded laser with a narrower spectral linewidth. With these improvements, as shown in Fig. 7, an *SNR* in the range of 50~70 should be obtainable. At the same time, using a more powerful laser to increase  $E/H$  will also enhance the *SNR* of the measurements.

## CONCLUSION

A novel flow visualization technique is described, demonstrated, and assessed in this paper. This technique utilizes PDS to overcome some of the limitations of existing techniques. The technique involves seeding a PD precursor, then completely and rapidly photodissociating it into photofragments. By carefully selecting a PD precursor that can produce a photofragment (e.g., an atomic species) with a strong LIF transition, this technique can provide even higher signal levels than existing PLIF techniques and can potentially simplify the interpretation of the signal because of the simple structure of the target photofragment. Based on these considerations, the PDS-based technique can potentially improve and expand the applications of LIF techniques (including PLIF and TPLIF).

This technique was assessed using  $I_2$  as an example precursor. A methodology was developed to concisely and clearly map out the interplay between various key factors of the new technique, including the rapidness and completeness of the PD process, the spatial resolution, signal strength, and size of the field of view. When applied to  $I_2$  precursor, this method provided a promising outlook for the technique as a practical flow visualization technique. With currently available laser and camera equipment, high *SNR* measurements can be obtained with rapid temporal resolution across a field of view on the order of centimeters. The technique was also experimentally demonstrated for the 2D measurement of the mixture fraction, further illustrating its advantages for such special applications. These advantages are expected to become more critical in reactive flows. At the same time, the experimental demonstration also provided test data to validate the assessment method developed. We expect this method to be useful for assessing other flow imaging techniques as well.

Experimental demonstration of the new technique for mixture fraction imaging in reactive flows is underway. However, the potential application areas of the PDS-based technique are not limited to mixture fraction measurements. For example, temperature measurement is also an attractive application. In this application, the temperature of the flow (either nonreactive or reactive) is obtained by measuring two LIF transitions of the target photofragment. Compared with existing two-line LIF thermometry, the PDS-based technique offers several distinct advantages. First, again, with a properly selected PD precursor, the target photofragment (e.g., the atomic I described here, or atomic Na with NaI as the PD precursor) can possess a strong LIF transition and a simple atomic structure for inferring temperature. Second, the PDS-based method can circumvent the use of established LIF

candidates such as OH and NO, which either do not exist naturally or are difficult to seed. Furthermore, in the case of temperature measurements, the PD precursor does not need to be completely photodissociated. The PD laser pulse only needs to produce enough photofragments to ensure a required *SNR*, which will further simplify the implementation and expand the applicable range of the PDS technique.

Before closing this paper, mention should be made of the potential difficulties of TPLIF imaging of atomic I. First, compared with single-photon LIF, interpretation of TPLIF signal is usually more complicated. Two approaches are being investigated to address this difficulty. The first approach, as mentioned above, seeks other PD precursors to generate photofragments that can be imaged by single-photon LIF. The second approach attempts to take advantage of the relatively large photoionization cross-section of atomic I to simplify the data interpretation. Second, another typical difficulty with TPLIF involves the use of high laser irradiance to enhance the signal level, which can trigger photochemical reactions and introduce interference. The use of TPLIF with atomic I is expected to be immune to such interference, because atomic I is foreign to most flows and therefore photochemical reactions do not generate spurious I atoms. However, the interference emissions near 804 nm caused by photochemical effects need to be examined.

## ACKNOWLEDGMENTS

This work was supported by a University Research Grant from Clemson University. We thank Jian Cai (Clemson University) for many valuable discussions during the course of this work. Special thanks are also due to an anonymous reviewer, whose comprehensive and critical review has helped to strengthen multiple aspects of this paper.

1. N. Peters, *Turbulent Combustion* (Cambridge University Press, Cambridge, UK, 2000).
2. R. S. Barlow, *Proc. Combust. Inst.* **31**, 49 (2007).
3. A. C. Eckbreth, *Laser diagnostics for combustion temperature and species* (Gordon and Breach Publishers, The Netherlands, 1996).
4. C. F. Kaminski and M. B. Long, “Multidimensional Diagnostics in Space and Time”, in *Applied Combustion Diagnostics*, K. Kohse-Hoinghaus and J. B. Jeffries, Eds. (Taylor & Francis, New York, 2002).
5. R. S. Barlow, C. D. Carter, and R. B. Pitz, “Multiscalar Diagnostics in Turbulent Flames”, in *Applied Combustion Diagnostics*, K. Kohse-Hoinghaus and J. B. Jeffries, Eds. (Taylor & Francis, New York, 2002).
6. W. Cai, D. J. Ewing, and L. Ma, *Comp. Phys. Commun.* **179**, 250 (2008).
7. L. Ma and W. W. Cai, *Appl. Opt.* **47**, 3751 (2008).
8. P. A. Davidson, *Turbulence - An Introduction for Scientists and Engineers* (Oxford University Press, Oxford, UK, 2004).
9. G. P. Smith, D. M. Golden, M. Frenklach, N. W. Moriarty, B. Eiteneer, M. Goldenberg, C. T. Bowman, R. K. Hanson, S. Song, W. C. Gardiner, Jr., V. V. Lissianski, and Z. Qin, “GRI-MECH 3.0,” [http://www.me.berkeley.edu/gri\\_mech/](http://www.me.berkeley.edu/gri_mech/) (2008).
10. V. Babushok, T. Noto, D. R. F. Burgess, A. Hamins, and W. Tsang, *Combust. Flame* **107**, 351 (1996).
11. A. McIlroy and L. K. Johnson, *Combust. Sci. Technol.* **116**, 31 (1996).
12. J. G. Calvert and J. N. Pitts, *Photochemistry* (John Wiley and Sons, New York, 1966).
13. H. Okabe, *Photochemistry of Small Molecules* (John Wiley and Sons, New York, 1978).
14. A. Saiz-Lopez, R. W. Saunders, D. M. Joseph, S. H. Ashworth, and J. M. C. Plane, *Atmos. Chem. Phys.* **4**, 1443 (2004).
15. J. Tellinghuisen and L. F. Phillips, *J. Phys. Chem.* **90**, 5108 (1986).
16. R. D. Clear and K. R. Wilson, *J. Mol. Spectrosc.* **47**, 39 (1973).
17. A. B. Alekseyev, H. P. Liebermann, D. B. Kokh, and R. J. Buenker, *J. Chem. Phys.* **113**, 6174 (2000).
18. L. H. Macdonald and R. L. Strong, *J. Phys. Chem.* **95**, 6940 (1991).
19. M. J. Rosker, M. Dantus, and A. H. Zewail, *Science* (Washington, D.C.) **241**, 1200 (1988).
20. K. McMillan, J. W. Bevan, and E. S. Fry, *J. Appl. Phys.* **61**, 4902 (1987).

21. H. Ooe, Y. Kimura, M. Terazima, and N. Hirota, *J. Phys. Chem. A* **103**, 7730 (1999).
22. J. Tellinghuisen, *J. Chem. Phys.* **58**, 2821 (1973).
23. G. Herzberg, *Molecular Spectra and Molecular Structure. Volume I - Spectra of Diatomic Molecules* (Krieger Publishing Company, Florida, 1950).
24. R. J. Le Roy, G. T. Kraemer, and S. Manzhos, *J. Chem. Phys.* **117**, 9353 (2002).
25. Y. J. Jung, Y. S. Kim, W. K. Kang, and K. H. Jung, *J. Chem. Phys.* **107**, 7187 (1997).
26. P. Brewer, P. Das, G. Ondrey, and R. Bersohn, *J. Chem. Phys.* **79**, 720 (1983).
27. J. J. Tiee, M. J. Ferris, G. W. Loge, and F. B. Wampler, *Chem. Phys. Lett.* **96**, 422 (1983).
28. S. T. Sanders, D. W. Mattison, L. Ma, J. B. Jeffries, and R. K. Hanson, *Opt. Exp.* **10**, 505 (2002).
29. N. J. Bednar, J. W. Walewski, and S. T. Sanders, *Appl. Spectrosc.* **60**, 246 (2006).
30. A. N. Karpets and R. S. Barlow, *Proc. Combust. Inst.* **30**, 665 (2005).
31. J. A. Sutton and J. F. Driscoll, *Exp. Fluids* **41**, 603 (2006).
32. G. J. Fiechtner and J. R. Gord, *J. Quant. Spectrosc. Radiat. Transfer* **68**, 543 (2001).
33. S. J. Davis, P. A. Mulhall, M. Bachman, W. J. Kessler, and P. B. Keating, *J. Phys. Chem. A* **106**, 8323 (2002).
34. V. N. Lokhman, D. D. Ogurok, and E. A. Ryabov, *Eur. Phys. J. D* **46**, 59 (2008).